Double-gap bicone magnetorheology in steady shear under homogeneous magnetic and flow fields

Guillermo Camacho, Juan de Vicente, and Jose R. Morillas*

F2N2Lab, Magnetic Soft Matter Group and Excellence Research Unit 'Modeling Nature' (MNat), Department of Applied Physics, Faculty of Sciences, University of Granada, C/Fuentenueva s/n, 18071 Granada, Spain

(Received 18 December 2023; accepted 3 July 2024; published 29 July 2024)

We design, fabricate, and test a double-gap bicone magnetorheological (MR) device to measure steady shear rheological properties of MR fluids under saturating magnetic fields (i.e., large enough to saturate the MR fluids). The device is optimized using finite element method and computational fluid dynamics simulations so that homogeneous, saturating field strengths are reached while keeping a constant shear rate within the main shearing gaps. Experiments demonstrate that the flow curves in the saturation regime can be fitted to a viscoplastic Casson model in good agreement with MR fluids under much lower (nonsaturating) fields. Moreover, yield stress data follow a linear dependence on volume fraction at low particle loadings, in agreement with existing theoretical models.

DOI: 10.1103/PhysRevResearch.6.033115

I. INTRODUCTION

Magnetorheological (MR) fluids of interest in applications are colloidal suspensions of magnetizable particles in a nonmagnetic liquid carrier. In the presence of external magnetic fields, the particles become magnetized and interact to form field-oriented aggregates that have a profound impact in the rheological behavior of the MR fluid promoting the appearance of a yield stress [1]. To fulfill the application requirements, current works on magnetorheology have pursued the development of more stable MR fluids with a larger yield stress. Such goals are fulfilled with synthesis routes that include non-Newtonian carriers and patchy, nonspherical and/or bidisperse particles [2,3].

Two key parameters control the yield stress of a conventional MR fluid (consisting of spherical and magnetically homogeneous particles in a Newtonian liquid carrier): the magnetic field strength H and the particle concentration ϕ [4–7]. The magnetic field strength determines the magnetization level of the particles. The larger the external magnetic field strength, the larger the magnetization of the particles, and therefore, the greater the interparticle magnetostatic force. Ideally, one would like to work in the magnetic saturation regime, when the magnetic field strength is large enough for the particle magnetization to reach the high field plateau. Unfortunately, this is not a simple task.

Magnetizable particles employed in the formulation of MR fluids are typically micron sized and made of carbonyl iron [8]. For these particles, the magnetization vs field strength curve fully saturates at a magnetic field strength of $H \sim 950$ kA m^{-1} [9], which is not easily accessible in conventional commercial MR devices. The highest magnetic field strength generated in a commercial single-gap device is $\sim$795 kA m^{-1} for both the Anton Paar [10] and TA [11] magnetocells. A larger field strength (1114 kA m^{-1}) can be achieved using the twin-gap device commercialized by Anton Paar [12]. Additionally, an important complication arises at high fields as the magnetic field strength loses homogeneity within the sample volume [12–14]. Generation of strong magnetic fields necessarily involves the use of electromagnetic circuits, and the presence of the shearing geometry implies drilling a hole through the upper yoke of the magnetocell that induces the undesired field inhomogeneity (e.g., see Fig. 5 in Ref. [13]).

With the purpose of achieving not only saturating but also homogeneous magnetic fields within the sample volume, Morillas *et al.* [15] proposed the use of a double-gap plate-plate device (see sketch in the Supplemental Material [16]). This setup, inspired by the twin-gap device previously proposed by Laun *et al.* [12], introduces another degree of freedom by changing the upper and bottom gaps at will. By simply displacing the plate upward, it is possible to match the averaged magnetic field in the upper and bottom gaps. Using a double-gap magnetocell device, Morillas and de Vicente [17] were capable of measuring the yield stress of MR fluids in saturation from particle concentrations as low as $\phi = 0.15$ up to particle concentrations of $\phi = 0.5$. The experimental results were successfully compared, especially at high loadings, with finite element method (FEM) simulations on model structures [17].

An important drawback of the double-gap device is that the shear rate is not homogeneous within the sample volume, like what happens with the classical plate-plate geometry. As a result, it is not possible to get steady shear rheological curves because the sample history changes within the volume, and

*Contact author: jmorillas@ugr.es

MR fluids are generally thixotropic [18]. Another handicap of the double-gap device is the long gaps it involves, which could prevent low-concentration suspensions spanning the whole volume when structured. In this paper, we explore the possibility of using a bicone (BC) instead of a flat plate. This is motivated by the fact that conical surfaces of sufficiently small angle produce narrow gaps and generate uniform shear rates [19]. The BC fabricated in the context of this paper is based on the double-gap plate-plate device already developed by Morillas *et al.* [15]. Our design preserves the remarkable magnetic properties of that device, and by the careful addition of nonmagnetic conical pieces, the geometry is improved to achieve homogeneous shear rates and to measure MR fluids of smaller particle concentrations.

II. MATERIALS AND METHODS

Nonmagnetic conical pieces used in the construction of the BC were three-dimensionally (3D) printed in a Stratasys Object30 using VeroWhite as the printing material. This device offers a maximum theoretical resolution of 16μm. These pieces were carefully glued onto the magnetic soft iron plate described by Morillas *et al.* [15] (Tool#2 in that reference) with a thin film of epoxy resin.

Carbonyl iron microparticles (EW grade) used in the formulation of the MR fluids were provided by BASF SE (Germany). Silicone oils (SO) of different viscosities (SO500: 0.489 Pa s, SO1000: 0.893 Pa s, SO10000: 9.76 Pa s, all of them measured at 25 °C) were obtained from Sigma-Aldrich and used without further purification. Ultrapure glycerol was provided by Fisher Scientific. MR fluids were prepared by vigorous dispersion of the iron microparticles in the oils or glycerol/water mixtures employing a centrifugal mixer.

Rheological tests were conducted using a commercial rheometer (MCR302, Anton Paar, Austria) with the double-gap BC geometry and a MRD 70/1T magnetocell (Anton Paar) attached to the rheometer base. Shear rate sweeps were carried out to construct the rheograms and viscosity curves, involving three essential steps: First, a preshear ($\dot{\gamma} = 350\,\mathrm{s}^{-1}$ during 10 s) was applied to delete any previous fluid history. Next, flow was removed, and a saturating magnetic field was suddenly imposed (structuration step) for 30 s. Finally, an angular velocity logarithmic ramp was performed, keeping the field magnitude and direction. Determination of the yield stress was done through a shear stress sweep, replacing the angular velocity ramp by a torque logarithmic ramp and identifying the yielding value with the shear stress responsible for a large jump in the measured shear rate (see Fig. S2 in the Supplemental Material [16]).

Both (shear rate and stress) sweeps were ascending (ramp up tests) to test the mechanical properties of the columnlike structure formed at rest. Descending sweeps are responsible for the appearance of different (layered) structures of no interest in this paper [20]. For validation purposes, tests on Newtonian fluids were repeated with a commercial cone-plate (CP) geometry (50 mm diameter, 1 ° angle, Anton Paar), skipping the structuration step and the magnetic field application.

The first goal was the design of a BC that fits within the housing used in the double-gap geometry. Figure 1 shows a schematic of the setup, where the magnetic pieces are highlighted in dotted gray colors. In our analysis, the radius of the rotor R_r is fixed to $R_r \leqslant 8$ mm because of the tolerances in the construction of the setup, and our free parameters are the distance to the bottom surface h_b and the nonmagnetic cone angle θ_0.

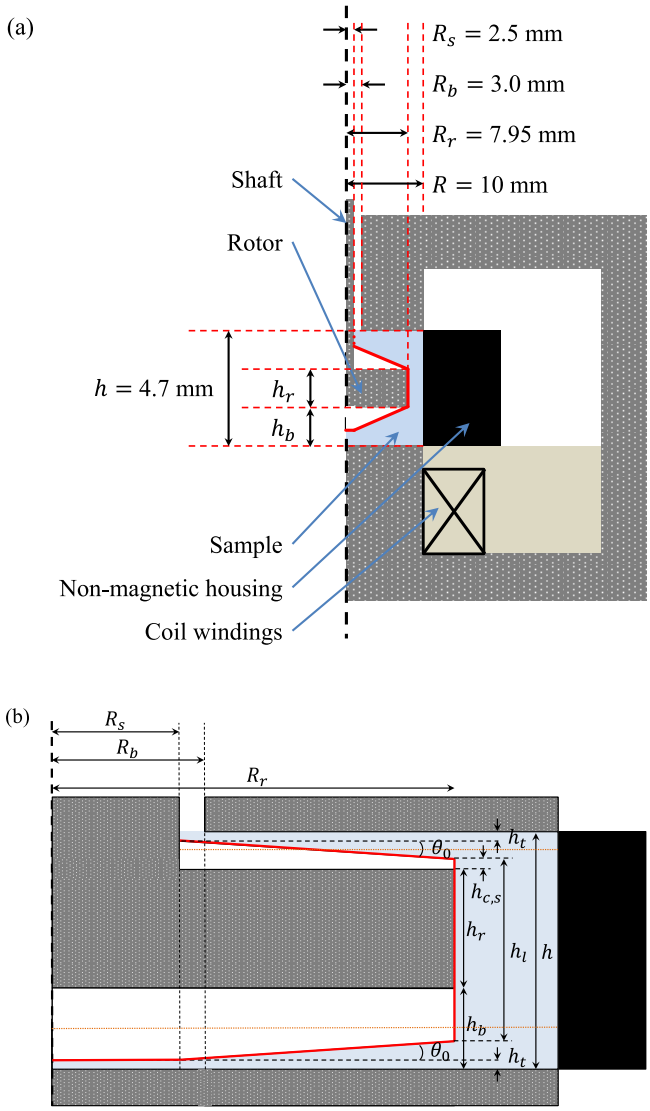

FIG. 1. Schematics of the double-gap bicone (BC). This design is a modification of the Anton Paar MRD 70/1T magnetocell including the commercial ferromagnetic spacer ring of thickness 1.29 mm. (a) Scheme of the whole magnetocell. (b) Zoomed picture of the shearing region to highlight the different components of the BC. Dotted gray colors correspond to ferromagnetic components, while the rest are nonmagnetic. Both figures have cylindrical symmetry around the black dashed axis.

Computational fluid dynamics (CFD) and magnetostatic FEM problems were solved using COMSOL Multiphysics to optimize the design of the device. Cauchy and continuity equations were solved in the stationary state within an axisymmetric domain enclosing the sample (light blue region in Fig. 1). The fluid domain was discretized using a structured regular mesh with a mean element size of 0.055 mm. The finer mesh was close to the rotor corner (mesh element size of 0.01 mm).

Numerical FEM simulations were also carried out to solve Maxwell's equations in the stationary state and compute the magnetic field distribution in the magnetocell. The axisymmetric plan is sketched in Fig. 1(a), and it includes the magnetic circuit (yokes), magnetic rotor, sample region, and energized coils. The magnetic properties of each piece were considered in these simulations through their *BH* curve. To simulate the nonmagnetic surroundings of the magnetocell and define the boundary conditions, the whole device was placed within a cylindrical box. On its boundaries, the normal component of the magnetic field was made zero. The height and radius of the box were $2.3h_{m,c}$ and $2r_{m,c}$, respectively, with $h_{m,c}$ and $r_{m,c}$ the height and radius of the magnetocell, respectively. A simulation box twice as large gave differences $<0.1\%$ discarding size effects. Regarding the mesh, simulations were carried out for finer and finer meshes until no significant difference was observed in the results. The mesh density changed depending on the computational domain region. The densest one was located within the gap between the yokes (mesh element size ~0.1 mm), while it became coarser as it went away from that position (0.5 mm in the yokes, 2 mm in the coil windings, and 14 mm in the external cylinder next to its boundaries).

III. NUMERICAL CALCULATION OF THE MAGNETIC FIELD STRENGTH

The use of a ferromagnetic BC is expected to allow the generation of homogeneous shear rates, but the resulting magnetic field would be inhomogeneous and not parallel to the rotation axis. In this section, we aim to find the optimal geometry that generates a uniform field within the measuring cell. In a previous study, we demonstrated that a strategically designed soft iron plate can generate a homogeneous and equal magnetic field above and below it [15]. This way, by adding nonmagnetic supplementary pieces, we can give the plate a biconical shape while preserving its homogeneous magnetic field distribution, resulting in the device shown in Fig. 1.

When the ferromagnetic plate is placed in the center of the magnetocell, leaving equal gaps above and below it, the magnetic field is larger in the bottom gap due to the central bore in the upper yoke. To address this issue, both the position of the plate within the measuring cell and its thickness can be adjusted. This allows the identification of an optimal position and size that produce homogeneous fields while maintaining a high field strength. A dimensionless number, referred to as the *change in magnetic field* (CMF), was defined to quantify the variation in the magnetic field within the gaps occupied by the sample:

$$\mathrm{CMF} = \frac{\bar{B}_b - \bar{B}_u}{\bar{B}_u}, \tag{1}$$

where $\bar{B}_b$ and $\bar{B}_u$ represent the averaged magnetic flux densities in the bottom and upper gaps, respectively:

$$\bar{B}_i = \frac{\int_V B_i(r,z)\, dV_i}{V_i}. \tag{2}$$

Here, the bottom gap volume V_b comprises the $r < R_r$ region below the plate, while the upper gap is integrated in the range $R_b < r < R_r$ above the plate.

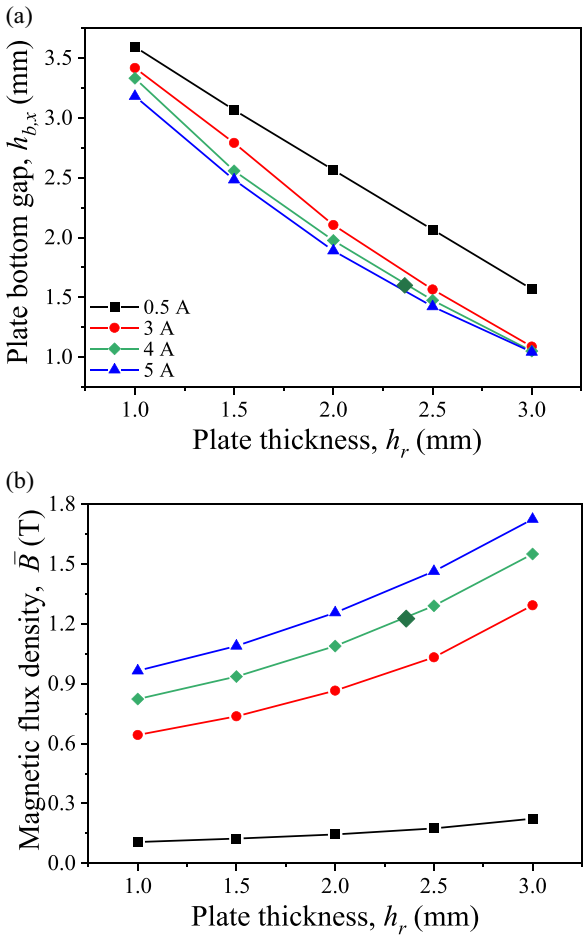

FIG. 2. (a) Magnetic plate distance to the bottom surface $h_{b,x}$ corresponding to CMF = 0 vs magnetic plate thickness h_r for four different currents (I = 0.5, 3, 4, and 5 A). (b) Magnetic flux density $\bar{B}$ for those positions and currents as a function of h_r.

FEM simulations were carried out to determine the magnetic field distribution in the shearing cell. First, to minimize the CMF for a given magnetic plate thickness h_r, we simply displace it upward. In Fig. 2(a), we show the bottom gap height $h_{b,x}$ (i.e., the distance from the lower surface of the plate to the bottom of the measuring cell) that makes CMF = 0 for a given h_r at different operating currents I. Figure 2(b) shows the averaged magnetic flux within the cell for the same h_r and I values. In this paper, we employed a soft iron plate with a thickness of $h_r = 2.36$ mm and a radius of $R_r = 7.95$ mm (Tool#2 in Ref. [15]), which based on Fig. 2(a), produces optimal performance at a working distance of $h_{b,x} = 1.6$ mm and a current of $I = 4$ A. This generates a magnetic flux density of $B_s = 1.23$ T and field strength of $H_s = 975$ kA m^{-1} [see Fig. 2(b)], which is sufficient to fully saturate carbonyl iron particles. The specific values selected in this paper are indicated in Fig. 2 with a dark-green diamond and will be fixed during the optimization of the BC dimensions (Sec. VI).

Thus far, we have discussed averaging fields in lower and upper gaps. However, the magnetic field is not only equal in both gaps but also constant along the radial direction. The absence of field gradients prevents particle migration

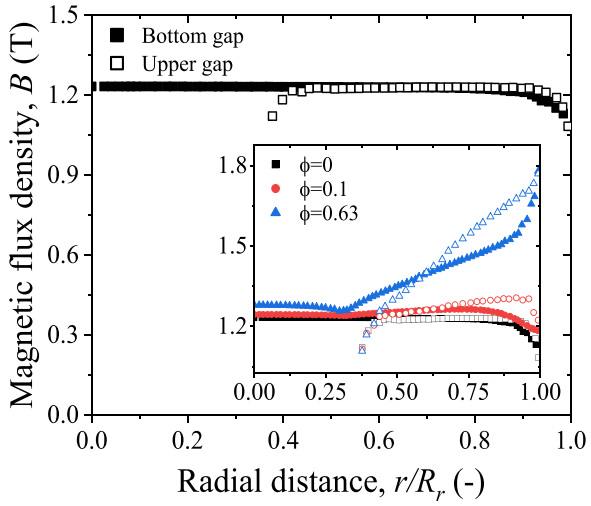

FIG. 3. Simulated magnetic flux density B as a function of the normalized radial position r/R_r for the fabricated geometry. B is computed in the middle height of each gap [orange dotted lines in Fig. 1(b)]. The coil is fed with a current of 4 A. The inset shows the magnetic flux density profile when the sample has a magnetization of ϕM_s for different volume fractions ϕ. Note that the maximum particle loading explored in this paper is $\phi = 0.1$.

due to magnetophoretic forces in this direction and ensures a homogeneous distribution of the field-induced structures [13]. In Fig. 3, the magnetic field profile along the radial position is shown for the fabricated geometry. The data reveal that the saturating value $B_s = 1.23$ T is achieved in the whole cell, with slight deviations at the rim due to edge effects. For more detailed information on magnetic field calculations and shape optimization, we refer to Morillas *et al.* [15].

It is also necessary to note that, when working with a magnetic sample, a discontinuity will arise at the boundary between the nonmagnetic conical surface and the MR fluid. This fact may compromise the homogeneity of the field along the plate radius, thus requiring an evaluation of its effect. The inset in Fig. 3 represents the FEM simulated magnetic field profile in the presence of a magnetic sample (instead of air) with magnetization ϕM_s, where $M_s = 1600$ kA m^{-1} is the saturation magnetization of the magnetic particles used in the experiments. As observed, for concentrations up to $\phi = 0.1$, which is the maximum concentration used in this paper, field homogeneity changes very little (maximum variation of 5%). This can primarily be attributed to the small cone angle and relatively low particle concentration. As expected, for very large concentrations, variations become larger, as shown in the inset of Fig. 3, for maximum packing. At very large concentrations, field homogeneity is compromised.

IV. ANALYTICAL CALCULATION OF THE SHEAR RATE AND SHEAR STRESS

The software controlling commercial rheometers provides raw data in terms of torque M and angular velocity Ω. Hence, to measure rheological material functions, it is necessary to derive analytical expressions for the torque–shear stress and angular velocity–shear rate relationships.

The torque acting on the BC due to the confined fluid can be computed by integrating the shear stress over its surface:

$$M = \int_S r\,\tau\,dS. \tag{3}$$

Following the procedure outlined in Morillas *et al.* [15], this torque can be obtained as the sum of four main contributions: (i) the truncation plate surface, (ii) the bottom cone, (iii) the upper cone, and (iv) the lateral surface [see red lines in Fig. 1(b)]. This last contribution is treated as two concentric cylinders, with the inner one rotating and the outer one at rest.

The shear rate on any of these surfaces can be expressed as a function of the angular velocity Ω, the cone angle θ_0, and the geometrical dimensions as follows:

$$\dot{\gamma}_{b,p}(r) = \frac{r\Omega}{h_t}, \tag{4a}$$

$$\dot{\gamma}_{b,c} = \frac{\Omega}{\theta_0}, \tag{4b}$$

$$\dot{\gamma}_{u,c} = \frac{\Omega}{\theta_0}, \tag{4c}$$

$$\dot{\gamma}_l = \frac{2\Omega}{1-(R_r/R)^2}. \tag{4d}$$

It is worth noting that the shear rate on the conical surfaces ($\dot{\gamma}_{b,c}$ and $\dot{\gamma}_{u,c}$) is calculated assuming the low-angle approximation, and only in this case is it appropriate to talk about a constant value.

To compute the integral in Eq. (3), it is necessary to assume a constitutive equation to write the shear stress τ in terms of the shear rate $\dot{\gamma}$ and, through Eqs. (4a)–(4d), the system parameters. In our case, we considered a general power-law fluid with variable flow behavior index. This model acts as a bridge between Newtonian and yield stress fluids of interest in this paper [21], capturing the initial yielding regime and the transition to the post-yield Newtonian behavior. The shear stress–shear rate relationship in the power-law constitutive model is given by

$$\tau = m\dot{\gamma}^n, \tag{5}$$

where m is the flow consistency index and n the flow behavior index. Therefore, introducing Eq. (5) into Eq. (3), we can perform the integration and compute the torque exerted on the BC as follows:

$$M = \int_{S_{b,p}} rm[\dot{\gamma}_{b,p}(r)]^n dS + \int_{S_{b,c}} rm[\dot{\gamma}_{b,c}(r)]^n dS + \int_{S_{u,c}} rm[\dot{\gamma}_{u,c}(r)]^n dS + \int_{S_l} rm[\dot{\gamma}_l(r)]^n dS, \tag{6}$$

where $S_{b,p}$, $S_{b,c}$, $S_{u,c}$, and S_l represent the surfaces of the bottom truncation plate, bottom cone, upper cone, and lateral cylinder, respectively. By substituting the expressions for the shear rate from Eqs. (4a)–(4d), we obtain

$$M = \int_{r=0}^{R_s}\int_{\varphi=0}^{2\pi} rm\left(\frac{r\Omega}{h_t}\right)^n rd\varphi dr + \int_{r=R_s}^{R_r}\int_{\varphi=0}^{2\pi} rm\left(\frac{\Omega}{\theta_0}\right)^n rd\varphi dr$$

$$+\int_{r=R_b}^{R_r}\int_{\varphi=0}^{2\pi} rm\left(\frac{\Omega}{\theta_0}\right)^n r d\varphi dr + \int_{h=0}^{h_l}\int_{\varphi=0}^{2\pi} R_r m\left(\frac{2\Omega}{1-(R_r/R)^2}\right)^n R_r d\varphi dh, \quad (7)$$

and integrating, we arrive at

$$M = 2\pi m\left\{\left(\frac{\Omega}{h_t}\right)^n \frac{R_s^{3+n}}{3+n} + \left(\frac{\Omega}{\theta_0}\right)^n \frac{2R_r^3 - R_b^3 - R_s^3}{3} + \left[\frac{2\Omega}{1-(R_r/R)^2}\right]^n R_r^2 h_l\right\}. \quad (8)$$

Finally, we can rewrite this equation in terms of the shear stress on the conical surfaces, as they represent the main contribution to the total torque. Bearing in mind that the stress in the cone is $\tau_c = m\dot{\gamma}_c^n = m(\frac{\Omega}{\theta_0})^n$, Eq. (8) reads as follows:

$$\tau_c = \frac{3M}{2\pi R_r^3}\left\{2 - \frac{R_b^3 + R_s^3}{3R_r^3} + \left(\frac{\theta_0}{h_t}\right)^n \frac{3}{3+n}\frac{R_s^{3+n}}{R_r^3} + \left[\frac{2\theta_0}{1-(R_r/R)^2}\right]^n \frac{3h_l}{R_r}\right\}^{-1}. \quad (9)$$

In the case of MR fluids in the preyield regime, the stress is constant and equal to the yield stress $\tau_c = \tau_y$. Consequently, the yield stress is obtained making $n = 0$ in Eq. (9):

$$\tau_y = \frac{3M}{2\pi R_r^3}\left[2 - \frac{R_b^3 + R_s^3}{3R_r^3} + \left(\frac{R_s}{R_r}\right)^3 + \frac{3h_l}{R_r}\right]^{-1}. \quad (10)$$

Furthermore, for MR fluids structured under an external field parallel to the rotor shaft, the lateral surface contribution can be safely neglected because the field-induced chainlike structures will not connect this surface to the lateral housing wall. Thus, Eq. (10) becomes

$$\tau_y = \frac{3M}{2\pi R_r^3}\left[2 - \frac{R_b^3 + R_s^3}{3R_r^3} + \left(\frac{R_s}{R_r}\right)^3\right]^{-1}. \quad (11)$$

Conversely, when the fluid behaves as a Newtonian liquid, Eq. (9) is simplified given that $m = \eta$ and $n = 1$, arriving at

$$\tau_c = \frac{3M}{2\pi R_r^3}\left\{2 - \frac{R_b^3 + R_s^3}{3R_r^3} + \frac{3\theta_0\, R_s^4}{4h_t R_r^3} + \frac{6\theta_0\, h_l}{R_r[1-(R_r/R)^2]}\right\}^{-1}. \quad (12)$$

Equations (11) and (12) provide useful expressions for the limiting behaviors corresponding to yield stress and Newtonian fluids, respectively. However, any intermediate rheological behavior can also be fitted by computing the local flow behavior index n, as described in Sec. VII.

V. NUMERICAL CALCULATION OF THE SHEAR RATE AND SHEAR STRESS

Non-Newtonian CFD was used to solve the fluid flow problem in the sample cell. The flow is governed by the Cauchy and continuity equations for laminar incompressible isothermal fluids in steady state neglecting body forces:

$$\rho(\vec{u}\cdot\nabla)\vec{u} = \nabla\cdot(-P\underline{\underline{I}} + \underline{\underline{\tau}}), \quad (13a)$$

$$\rho\nabla\cdot\vec{u} = 0. \quad (13b)$$

Here, ρ is the density of the fluid, $\vec{u}$ is the flow velocity, P is the pressure, $\underline{\underline{I}}$ is the identity tensor, and $\underline{\underline{\tau}}$ is the viscous stress tensor. A power-law constitutive model is assumed for the simulated fluid:

$$\underline{\underline{\tau}} = \eta(\dot{\gamma})\,\underline{\underline{\dot{\gamma}}}, \quad (14)$$

where $\eta = m\dot{\gamma}^{n-1}$ is the shear viscosity, $\underline{\underline{\dot{\gamma}}} = \nabla\vec{u} + (\nabla\vec{u})^T$ the shear rate tensor, and $\dot{\gamma} = \sqrt{\underline{\underline{\dot{\gamma}}} : \underline{\underline{\dot{\gamma}}}/2}$ the magnitude of $\underline{\underline{\dot{\gamma}}}$. However, it is noteworthy that all CFD results presented in the following section are restricted to the Newtonian case, as no significant differences were appreciated.

To solve Eqs. (13a) and (13b), we assumed the following boundary conditions:

(i) No-slip condition in the outer walls of the sample cell (i.e., housing and yokes):

$$\vec{u}_{\text{wall}} = \vec{0}; \quad (15a)$$

(ii) No-slip condition in the rotating wall (i.e., over the rotor surface):

$$\vec{u}_{\text{rot}} = \Omega r\,\hat{\theta}; \quad (15b)$$

(iii) Zero normal force in the gap of the shaft bore:

$$\vec{f}_0 = \vec{0}. \quad (15c)$$

With these, flow equations [Eqs. (13a) and (13b)] are solved to obtain the velocity $\vec{u}$ and pressure P fields, and the stress tensor is computed using Eq. (14). Eventually, the torque exerted on the rotor can be calculated like in the previous section, integrating Eq. (3) over the rotor surface.

VI. OPTIMIZING THE BC DIMENSIONS

Flow equations were solved to maximize the homogeneity in the shear rate field along the shearing gap. For this aim, CFD simulations were performed testing a wide range of conical geometries and computing the differences with the expected theoretical shear rate in the whole sample volume. To quantify these errors, a *shear rate reduced variance* was defined as follows:

$$\sigma^2 = \frac{\int_V (\dot{\gamma} - \dot{\gamma}_0)^2 dV}{\int_V \dot{\gamma}_0^2 dV}. \quad (16)$$

Here, $\dot{\gamma}$ is the magnitude of the shear rate tensor computed by CFD, and $\dot{\gamma}_0$ is the analytical value as given by Eqs. (4a)–(4d).

As a result of the magnetic field optimization, the bottom gap distance was fixed to $h_{b,x}$. Also, because of symmetry with the upper gap and to avoid frictional contacts with the lower yoke, the truncation radius was fixed to R_s. Consequently, at this stage, the only free parameter in the optimization of the BC dimensions is the subtended angle of the conical surfaces with the horizontal line θ_0 [see Fig. 1(b)]. Figure 4 shows the shear rate reduced variance σ^2 as a function of the cone angle θ_0. The main error contribution comes from the lateral surface σ^2_{lat} because Eq. (4d) is only valid for long cylinders in close approach, while the discrepancies between simulations and analytical predictions in the conical surfaces σ^2_{cone} are orders of magnitude below. As a result, shortening the lateral surface (i.e., increasing θ_0) reduces its contribution and

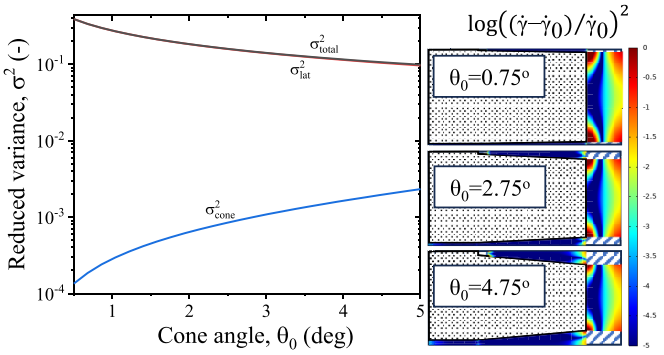

FIG. 4. Error estimation of the shear rate σ^2 as a function of the bicone angle θ_0. Contributions from the conical and lateral surfaces are distinguished. The total reduced variance is computed by addition of both contributions. Inset pictures show computational fluid dynamics (CFD) colormaps of the local shear rate reduced variance for three different cone angles ($\theta_0 = 0.75°$, 2.75°, and 4.75°).

makes σ^2 decrease until it reaches a minimum at large angles ($\theta_0 = 15°$, not shown), when the variance due to the conical surfaces becomes the most relevant one ($\sigma^2_{\text{cone}} > \sigma^2_{\text{lat}}$).

Obviously, for such a large θ_0, the low-angle approximation breaks, and the shear rate becomes inhomogeneous, so smaller θ_0's are needed. Furthermore, large angles also imply too-thin BCs (with lateral lengths shorter than the magnetic plate thickness h_r) and too-thin conical supplements. As noted in Sec. II, the BC is manufactured by glueing nonmagnetic conical supplements to the bottom and upper surfaces of the magnetic plate. To be 3D printed and remain mechanically stable when glued, those supplements need to have a minimum thickness. A thickness of $h_{c,s} = 0.18$ mm [see Fig. 1(b)] was found to be the minimum workable one that finally yielded a cone angle of $\theta_0 = 4°$ and a truncation gap of $h_t = 0.175$ mm. Table I summarizes the dimensions of the fabricated device. Finally, color maps in Fig. 4 display the local shear rate reduced variance over the volume in logarithmic scale. The shear rate in the region confined between the conical surfaces matches the analytical expression, except for the small border effects, up to order 10^{-4} in view of the color scale. Higher deviations are observed in the lateral zone, especially near the plate border and the housing wall.

To get better insight into the variation of the shear rate in the cell, Fig. 5 shows the reduced shear rate $\dot{\gamma}/\Omega$ as a function

TABLE I. Dimensions of the double-gap BC geometry.

Parameter	Measurement
Cell radius (R)	10.0 mm
Cell height (h)	4.7 mm
Bore radius (R_b)	3.0 mm
Shaft radius (R_s)	2.5 mm
Magnetic plate radius (R_r)	7.95 mm
Magnetic plate thickness (h_r)	2.36 mm
Magnetic bottom gap ($h_{b,x}$)	1.6 mm
Total lateral thickness (h_l)	3.59 mm
Truncation gap (h_t)	0.175 mm
Cone angle (θ_0)	4°

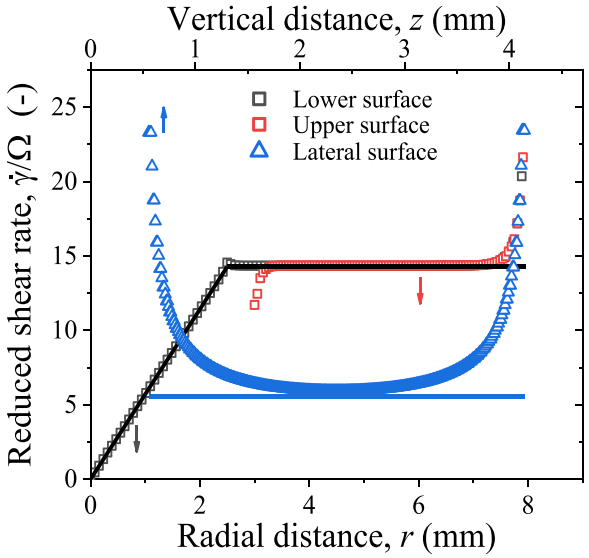

FIG. 5. Reduced shear rate ($\dot{\gamma}/\Omega$) as a function of the radial r (vertical z) distance on the conical (lateral) surfaces for the fabricated geometry. Solid lines represent the theoretical expressions for the reduced shear rate on different surfaces, computed following Eq. (4) and assuming a Newtonian constitutive equation. Symbols represent computational fluid dynamics (CFD) simulation results computed for a Newtonian fluid with viscosity 1 Pa s, sheared at an angular speed of $\Omega = 1\ \text{s}^{-1}$.

of the radial r (vertical z) distance along the conical (lateral) surface for the fabricated geometry. The agreement between analytical calculations and numerical simulations is very good for the conical surfaces. As expected, deviations are observed at the rim of the cone and near the shaft due to edge effects. In the case of the lateral surface, the agreement is not so good because the shear rate between concentric cylinders is strictly constant only in the narrow gap limit ($R_r/R \to 1$) and for long cylinders ($h_l \gg R$), which is not our case. Moreover, there exists a dependence on the constitutive equation that is also neglected [22]. Nevertheless, relative errors for the lateral surface are <6% in the central position and, considering the results presented in the following section, no substantial errors emerge when comparing the experimental, analytical, and simulated torques. Finally, it is also worth noting that, out of this lateral surface, well inside the sample, border effects are minimized, resulting in a greater degree of homogeneity for the shear rate, as seen in the color maps of Fig. 4.

VII. EXPERIMENTAL VALIDATION WITH NEWTONIAN FLUIDS

To test the validity of the BC device, experiments were conducted using Newtonian fluids. Silicone oils were chosen for this purpose because they are Newtonian at typical temperatures and shear rates [23], and their viscosity, density, and surface tension can be precisely controlled.

First, we compare both analytical calculations and simulations for the BC geometry with experimental measurements. In Fig. 6(a), the torque M dependence on angular velocity Ω is plotted. These are the raw data measured by the rheometer and can be directly compared with analytical equations [Eq. (8)]

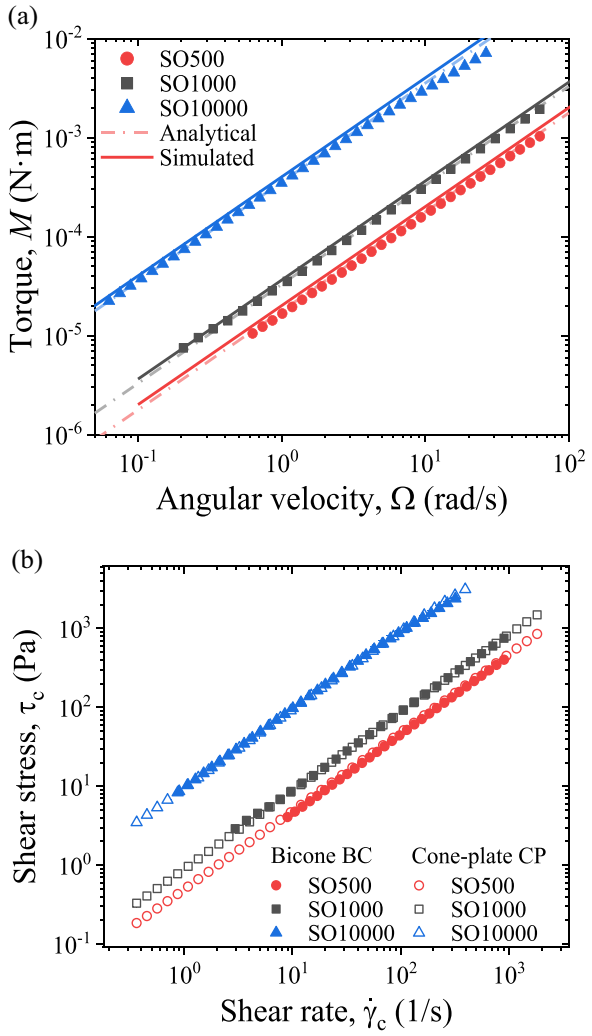

FIG. 6. Validation of the fabricated geometry for three silicone oils (SO500, SO1000, and SO10000) employed as model of Newtonian fluids. (a) Torque M vs angular velocity Ω curves. Symbols correspond to experimental measurements. Solid lines correspond to computational fluid dynamics (CFD) simulations assuming a Newtonian fluid with the same viscosity η as measured with the cone-plate (CP) geometry. Dashed lines are obtained using the analytical expression [Eq. (8)] assuming a Newtonian fluid with $n = 1$ and $m = \eta$. (b) Constitutive curves (shear stress vs shear rate) for the Newtonian fluids measured with a commercial CP geometry (open symbols) and the proposed bicone (BC) geometry (filled symbols).

and CFD simulations, assuming a Newtonian behavior with $n = 1$ and $m = \eta$, the viscosity of the fluid (measured with the CP geometry). The results show good agreement between the experimental, analytical, and simulated data for the three investigated fluids, which supports the effectiveness of our predictions.

The constitutive curve can be obtained from the data shown in Fig. 6(a). In Fig. 6(b), we show the shear stress τ_c vs shear rate $\dot{\gamma}_c$ at the conical surface. Filled symbols represent values measured in the BC device, while open symbols are measurements with the commercial CP geometry. Again, there is good agreement between both sets of measurements, which demonstrates that conversion from torque (angular velocity) to shear stress (shear rate) is done correctly using Eq. (9). It is worth noting that no assumptions about the Newtonian behavior of the fluid were made *a priori* for the measured data. Instead, the conversion from torque to shear stress is computed using a local value of the flow behavior index n, which is dependent on the angular velocity following $n = d\ln(M)/d\ln(\Omega)$. Despite this, a nearly Newtonian behavior is obtained as expected, with n values [i.e., the slope in Fig. 6(a)] always close to unity. The only exception is observed in high-molecular-weight silicone oils at elevated shear rates, where a minor shear-thinning effect is appreciated, as previously reported in the literature [24]. The viscosity plot is also provided in the Supplemental Material [16].

VIII. STEADY SHEAR FLOW CURVES IN SATURATED MR FLUIDS

Testing the BC geometry with Newtonian fluids enabled us to verify the calibration accuracy of the device. However, our primary objective was to study the behavior of MR fluids under saturating magnetic fields using all advantages the BC device features with respect to the commonly/previously used geometries in magnetorheology (e.g., plate-plate and double-gap ones). Namely, employing a conical geometry provides a more accurate measurement of the sample constitutive equation if compared with a plate-plate one. This is so because the cone creates a uniform shear rate field in the bottom and upper gaps and minimizes the impact of the mechanical history of the sample on the measurements.

Contrary to the common CP geometry, the shear stress measured in our BC device depends on the fluid constitutive equation through the flow behavior index n. This comes from the truncation plate and lateral surfaces and appears in the third and fourth terms inside the curly brackets of Eq. (9). Nevertheless, this dependence is not very strong. First, due to the short shaft radius, the truncation plate term is $<2\%$ of the conical surface ones (two first terms inside the curly brackets) even in the worst case ($n = 0$). Secondly, in the case of MR fluids, the field-induced structures are expected to grow in the rotating axis direction. Thus, they are parallel to the lateral surface, are not strained by the flow field, and consequently, give rise to a negligible shear stress on that surface.

Another important advantage of the BC geometry is its smaller sample gap if compared with the double-gap case. In a homogeneous, saturating magnetic field, the double-gap geometry requires sample gaps as large as 1.36 mm. In MR fluids, this can be an issue when working at low particle volume fractions because field-induced structures could not span the whole gap, leading to a lower-than-expected yield stress [25]. Therefore, accurate double-gap measurements are limited to volume fractions $\phi \gtrsim 0.15$ [26]. In contrast, the BC geometry has a gap of only $h_t = 0.175$ mm in the truncated apex, growing up to 0.56 mm at the rim. In the worst case, the sample gap in the BC is 2.5 times smaller than in the double gap, making it particularly suitable for working at low particle volume fractions as demonstrated below.

Figure 7(a) shows the flow curves for two different MR fluids prepared by dispersion of carbonyl iron in SO10000 at 0.3% and 1% particle volume fractions. Both curves were initially measured in the absence of an external magnetic

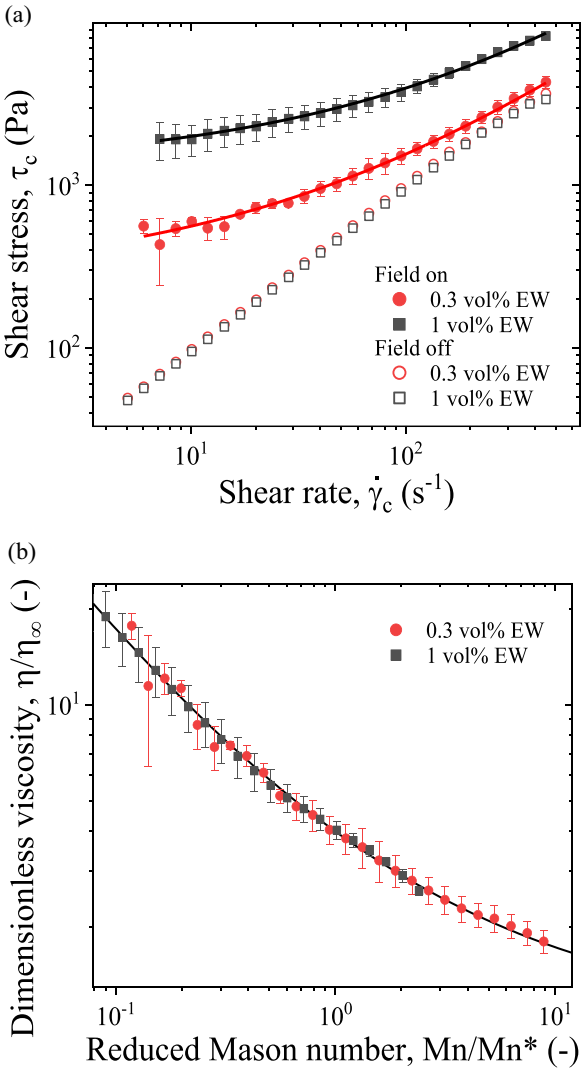

FIG. 7. Flow and viscosity curves of silicone oil SO10000-based magnetorheological (MR) fluids at 0.3 and 1 vol. % concentration. MR fluids were structured under a continuous saturating magnetic field and measured in the bicone (BC). (a) Shear stress vs shear rate without applied field (empty symbols) and at a saturating magnetic field (filled symbols). Solid lines correspond to a Casson model fit for the yielding fluids. (b) Dimensionless viscosity η/η_∞ vs reduced Mason number Mn/Mn* for both particle suspensions at saturating magnetic fields. The solid line corresponds to the universal master curve [Eq. (17)].

field, exhibiting a behavior very similar to that of the carrier fluid alone because of the low concentration of the particulate phase. The particle contribution to the stress is negligible when compared with the viscous stress of the carrier.

Next, a saturating magnetic field H_s is applied to the sample. This external magnetic field causes interparticle aggregation due to the emergence of magnetostatic interactions resulting in a yield stress. The yield stress is manifested by a low shear plateau in the shear stress vs shear rate curve [see Fig. 7(a)]. By gradually increasing the shear rate the field-induced structure is progressively broken, and the sample begins to flow until the rheogram matches the field-off curve in the high shear rate regime.

These flow curves encompass the preyield and postyield regimes of MR fluids under a homogeneous saturating magnetic field and a homogeneous shear rate profile. Many challenges had to be overcome to observe the solid-liquid transition. First and most important, saturating magnetic fields generate strong interparticle forces and therefore a very large particle contribution to the total stress that is typically orders of magnitude larger than the carrier liquid contribution. Second, commercial rheometers are limited to maximum measurable torques and angular speeds that do not typically allow the observation of the high shear viscosity plateau. Finally, for small particle concentrations, field-induced structures are not capable of spanning the whole sample gap.

Matching magnetostatic and hydrodynamic contributions at measurable stresses can be achieved by either reducing the particle content and/or increasing the viscosity of the carrier. There is a linear relationship between the particle stress and the particle volume fraction ϕ (at low ϕ) as well as between the viscous stress of the carrier and the shear rate assuming a Newtonian response. In this paper, we interrogate particle concentrations in the range $\phi \sim 0.01$–0.1 and high viscosity Newtonian carriers $\eta \sim 10$ Pa s.

Flow curves were fitted to a Casson plastic equation, which is represented by the solid lines in Fig. 7(a). This equation is given by $\tau^{1/2} = \tau_y^{1/2} + (\eta_\infty \dot{\gamma})^{1/2}$, where τ_y is the dynamic yield stress and η_∞ the high shear viscosity. Even though it only has two fitting parameters, the Casson model provides a more gradual transition from the yield to the Newtonian region than the Bingham model and has been demonstrated to fit the shear response of conventional MR fluids better [27], at least in the magnetic linear regime. Once τ_y and η_∞ have been determined by model fitting, data can be collapsed onto a single master curve, as shown in Fig. 7(b), which expresses the dimensionless viscosity (η/η_∞) as a function of the Mason number (Mn):

$$\frac{\eta}{\eta_\infty} = 1 + \left(\frac{\mathrm{Mn}}{\mathrm{Mn}^*}\right)^{-1} + 2\left(\frac{\mathrm{Mn}}{\mathrm{Mn}^*}\right)^{-1/2}. \qquad (17)$$

The Mason number is defined as $\mathrm{Mn} = \frac{72\eta_c\dot{\gamma}}{\mu_0\mu_{\mathrm{cr}}\langle M\rangle^2}$ and is the ratio between hydrodynamic and magnetostatic interactions [28,29]. Here, $\langle M\rangle$ is the average magnetization of the particles, which turns to be the saturation magnetization M_s in this case, μ_0 is the permeability of the vacuum, $\mu_{\mathrm{cr}} = 1$ is the relative permeability of the carrier fluid, and η_c its viscosity. Here, $\mathrm{Mn}^* = \frac{72\tau_y}{\mu_0\mu_{\mathrm{cr}}\langle M\rangle^2}\frac{\eta_c}{\eta_\infty}$ is the critical Mason number and demarcates the transition from magnetostatic to hydrodynamic control of the suspension structure. It solely depends on the particle volume fraction through the dynamic yield stress τ_y (note that, in the saturation and diluted regimes, neither $\langle M\rangle$ nor η_∞ is expected to introduce any additional dependence on ϕ). The good fit provided by the master curve of Eq. (17) and the particular values of Mn* (see next section) obtained in these experiments agree with previously reported viscosity curves for conventional MR fluids in the linear regime [30,31], extending the theoretical framework of the latter to the saturation and low-concentration regimes.

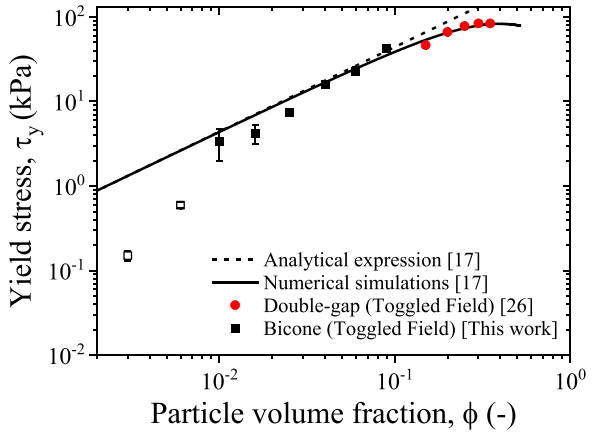

FIG. 8. Static yield stress τ_y as a function of particle volume fraction ϕ under saturating magnetic fields. Squares correspond to experiments from this paper (values from nonpercolating structures are marked with open symbols). Previously reported values for higher particle loadings are also plotted (circles), measured with the double-gap device applying toggled fields. The solid line corresponds to finite element method (FEM) simulations at saturation, and the dashed one is the asymptotic behavior $\tau_y \approx 0.137\mu_0 M_s^2\phi$ at low volume fractions [17].

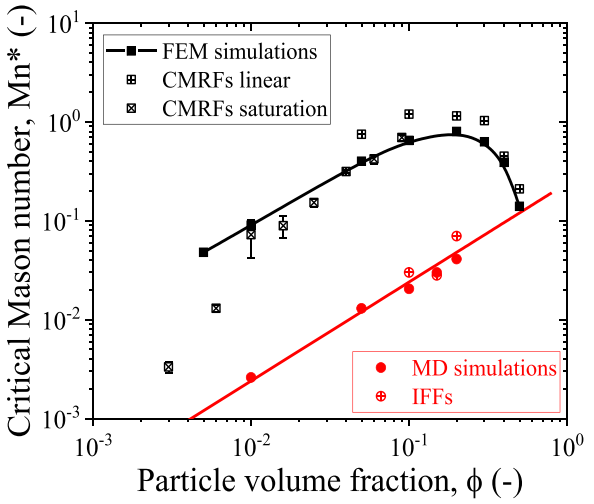

FIG. 9. Critical Mason number Mn∗ as a function of the particle volume fraction ϕ. × squares correspond to values obtained from the static yield stress measured in this paper. Previously reported values for conventional magnetorheological (MR) fluids (CMRFs) at linear regime (+ squares), finite element method (FEM) simulations (solid squares), inverse ferrofluids (IFFs; + circles) and molecular dynamics simulations (MD; solid circles) are also included [37,38]. Solid red line corresponds to the linear fit of IFFs and MD simulations, $\mathrm{Mn}^* = 0.24\phi$, as obtained by Ref. [37].

IX. YIELD STRESS IN SATURATED MR FLUIDS

Apart from generating the full flow curve of MR fluids under homogeneous and saturating magnetic fields, the BC geometry operates under narrow gaps and is therefore especially useful to measure at small and intermediate volume fractions, where the double-gap geometry fails to give accurate yield stress data. We also performed an extensive investigation on the dependence of the saturating yield stress with particle loading in this small-to-intermediate concentration regime.

In a previous work, a theoretical model for the yield stress at saturation was developed [17]. This model predicts that the dependence of the yield stress on particle volume fraction is linear at small particle loadings (also in agreement with models in the linear magnetization regime [32–35]), $\tau_y \approx 0.137\mu_0 M_s^2\phi$. However, for very large concentrations the yield stress levels off. Very good agreement with the theoretical model was obtained with carefully conducted experiments on MR fluids that were structured under the superposition of toggled magnetic fields instead of the conventional continuous steady fields [26]. The rationale behind this is that the theoretical model assumes the formation of a crystalline structure under the field, and this kind of structure is more closely formed by allowing particle rearrangements, due to Brownian motion, during the field-off periods of toggled fields.

In Fig. 8, we show yield stress measurements for different volume fractions together with previously reported data. Samples were prepared by suspending carbonyl iron particles in a 1:1 mixture of water and glycerol with a viscosity of 4.7 mPa s. This low-viscosity carrier fluid was chosen to allow particle diffusion during the application of the toggled field and the subsequent rearrangement of the structures. Magnetic pulses of 4 s were applied for 120 s during the structuration step to reduce defects in the chain structures (this protocol was found optimal in Ref. [26]), hence increasing yield stress of the sample [26], just before applying a continuous steady magnetic field during the shearing step. Data in Fig. 8 show that the saturating yield stress grows linearly with the volume fraction from $\phi \geqslant 0.01$ up to values of $\phi \approx 0.1$. In this loading range, there is good agreement between the theoretical prediction, numerical simulations, and experiments. Note that the particle loading range is one order of magnitude wider than the one explored with the double-gap geometry [26]. As observed in Fig. 8, the yield stress dramatically decreases for concentrations below $\phi = 0.01$ because particle structures are presumably not capable of connecting the conical surfaces.

Yield stress data reported in Fig. 8 can help us understand the volume fraction dependence of the critical Mason number Mn^*. Even though Mn^* is defined in terms of the dynamic yield stress τ_y, the latter can be safely approximated by the static yield stress, given the good agreement between FEM simulations and experiments [36] and the similar values measured under stress- and strain-controlled experiments [37]. A Quemada-like expression was used for the calculation of the high shear rate viscosity: $\eta_c/\eta_\infty = (1-\phi/\phi_0)^2$, where ϕ_0 is the maximum packing fraction for spheres, assumed to be $\phi_0 = 0.64$. In any case, this correction is not expected to be significant in our dilute MR fluids because $\eta_\infty \approx \eta_c$ in view of the flow curves. In Fig. 9, we show the calculated Mn^* values at different volume fractions along with previously studied experimental systems [conventional MR fluids (CMRFs) in the linear regime and inverse ferrofluids (IFFs)] and simulations [FEM and molecular dynamics (MD)]. According to Fig. 9, FEM simulations show much better agreement with experiments than MD for MR fluids, while the behavior of IFFs is well explained by the latter. Both IFFs and MR fluids

present a linear dependence (at least at low volume fractions) although their Mn^* values differ by more than an order of magnitude. Deviations at $\phi < 0.01$ for MR fluids were attributed to wall slip in nontexturized plates [36]. At large volume fractions, linearity is broken, and Mn^* decreases. This is a direct consequence of the yield stress being a continuous function of the concentration (explained through the FEM model in Ref. [17], see Fig. 4) and the viscosity diverging at the maximum packing (as it is empirically captured by the Quemada expression).

X. CONCLUSIONS

In this paper, we have designed and built a BC device that can generate homogeneous saturating magnetic fields and a constant shear rate profile. In this way, common artifacts in commercial devices (such as particle migration or ill-defined shearing history) are avoided. By only employing a strategically placed ferromagnetic plate, we can generate magnetic fields >1 T while maintaining good homogeneity within the measuring volume (maximum variation of 5%). Additionally, we demonstrate that the addition of nonmagnetic conical supplements to the plate provides the desired shear rate homogeneity.

Using the BC device, flow curves under saturating magnetic fields have been reported, revealing that they can be fitted to a Casson master curve following a similar behavior previously found in the literature for weaker magnetic fields. Consequently, it can be deduced that shear and magnetostatic forces are the two prevailing ones in this regime as well. Furthermore, low and intermediate particle concentrations can be measured with this device because the working gaps are lower than those employed in conventional plate-plate geometries and the field-induced structures can easily connect the biconical surfaces. This allowed us to demonstrate a linear dependence of the saturating yield stress with the volume fraction in the range from $\phi = 0.01$ to 0.1.

ACKNOWLEDGMENTS

We acknowledge P. Villalba González for preliminary CFD simulations on this project and G. Rus for 3D printing the nonmagnetic pieces used in the construction of the BC. This paper was supported by Projects No. PID2022-138990NB-I00 and No. TED2021.129384B.C22 funded by MCIN/AEI/10.13039/501100011033 and by EU NextGenerationEU/ PRTR. G.C. acknowledges the financial support by the FPU20/04357 fellowship. This project has received funding from the European Union's Horizon 2020 research and innovation programme under the Marie Skłodowska-Curie Grant Agreement No. 101030666.

[1] J. R. Morillas and J. de Vicente, Magnetorheology: A review, Soft Matter **16**, 9614 (2020).

[2] S. Odenbach, Magnetic hybrid materials, Arch. Appl. Mech. **89**, 1 (2019).

[3] Q. Lu, K. Choi, J. Nam, and J. C. Hyoung, Magnetic polymer composite particles: Design and magnetorheology, Polymers **13**, 512 (2021).

[4] M. Osial, A. Pregowska, M. Warczak, and M. Giersig, Magnetorheological fluids: A concise review of composition, physicochemical properties, and models, J. Intell. Mater. Syst. Struct. **34**, 1864 (2023).

[5] H. Khajehsaeid, N. Alaghehband, and P. K. Bavil, On the yield stress of magnetorheological fluids, Chem. Eng. Sci. **256**, 117699 (2022).

[6] G. Bossis, O. Volkova, Y. Grasselli, and A. Ciffreo, The role of volume fraction and additives on the rheology of suspensions of micron sized iron particles, Front. Mater. **6**, 4 (2019).

[7] A. Ghaffari, S. H. Hashemabadi, and M. Ashtiani, A review on the simulation and modeling of magnetorheological fluids, J. Intell. Mater. Syst. Struct. **26**, 881 (2015).

[8] *Magnetorheology: Advances and Applications*, edited by N. M. Wereley (The Royal Society of Chemistry, Cambridge, 2014).

[9] A. J. F. Bombard, I. Joekes, M. R. Alcântara, and M. Knobel, Magnetic susceptibility and saturation magnetization of some carbonyl iron powders used in magnetorheological fluids, Mater. Sci. Forum **416–418**, 753 (2003).

[10] J. Laeuger, K. Wollny, H. Stettin, and S. Huck, A new device for the full rheological characterization of magneto-rheological fluids, Int. J. Mod. Phys. B **19**, 1353 (2005).

[11] M. Ocalan and G. H. McKinley, High-flux magnetorheology at elevated temperatures, Rheol. Acta **52**, 623 (2013).

[12] H. M. Laun, C. Gabriel, and Chr. Kieburg, Twin gap magnetorheometer using ferromagnetic steel plates—Performance and validation, J. Rheol. **54**, 327 (2010).

[13] H. M. Laun, G. Schmidt, C. Gabriel, and C. Kieburg, Reliable plate-plate MRF magnetorheometry based on validated radial magnetic flux density profile simulations, Rheol. Acta **47**, 1049 (2008).

[14] B. K. Singh and C. Sarkar, Design, development, and performance analysis of plate-plate hybrid magneto rheometer considering uniform radial magnetic flux, J. Magn. Magn. Mater. **590**, 171691 (2024).

[15] J. R. Morillas, J. Yang, and J. de Vicente, Double-gap plate-plate magnetorheology, J. Rheol. **62**, 1485 (2018).

[16] See Supplemental Material at http://link.aps.org/supplemental/10.1103/PhysRevResearch.6.033115 for the sketch of the double-gap geometry, a typical yield stress measurement in a shear stress sweep experiment, and the viscosity plot of the fluids employed for calibration.

[17] J. R. Morillas and J. de Vicente, Magnetorheology in saturating fields, Phys. Rev. E **99**, 062604 (2019).

[18] J. de Vicente and C. L. A. Berli, Aging, rejuvenation, and thixotropy in yielding magnetorheological fluids, Rheol. Acta **52**, 467 (2013).

[19] C. W. Macosko, *Rheology: Principles, Measurements and Applications* (Wiley-VCH, Weinheim, 1994).

[20] O. Volkova, S. Cutillas, and G. Bossis, Shear banded flows and nematic-to-isotropic transition in ER and MR fluids, Phys. Rev. Lett. **82**, 233 (1999).

[21] H. A. Barnes and K. Walters, The yield stress myth? Rheol. Acta **24**, 323 (1985).
[22] I. M. Krieger and S. H. Maron, Direct determination of the flow curves of non-Newtonian fluids, J. Appl. Phys. **23**, 147 (1952).
[23] Y. Fan and K. Wang, The viscosity of dimethyl silicone oil and the concentration of absorbed air, AlChE J. **57**, 3299 (2011).
[24] D. Hadjistamov, Determination of the onset of shear thinning of polydimethylsiloxane, J. Appl. Polym. Sci. **108**, 2356 (2008).
[25] B. J. de Gans, N. J. Duin, D. V. D. Ende, and J. Mellema, Influence of particle size on the magnetorheological properties of an inverse ferrofluid, J. Chem. Phys. **113**, 2032 (2000).
[26] G. Camacho, J. R. Morillas, and J. de Vicente, Enhancing magnetorheology through the directed self-assembly under toggled magnetic fields in saturation, Smart Mater. Struct. **30**, 105029 (2021).
[27] C. L. A. Berli and J. de Vicente, A structural viscosity model for magnetorheology, Appl. Phys. Lett. **101**, 021903 (2012).
[28] O. Volkova, G. Bossis, M. Guyot, V. Bashtovoi, and A. Reks, Magnetorheology of magnetic holes compared to magnetic particles, J. Rheol. **44**, 91 (2000).
[29] D. J. Klingenberg, J. C. Ulicny, and M. A. Golden, Mason numbers for magnetorheology, J. Rheol. **51**, 883 (2007).
[30] J. A. Ruiz-López, R. Hidalgo-Alvarez, and J. de Vicente, Towards a universal master curve in magnetorheology, Smart Mater. Struct. **26**, 054001 (2017).
[31] K. Shahrivar, J. R. Morillas, Y. Luengo, H. Gavilan, P. Morales, C. Bierwisch, and J. de Vicente, Rheological behavior of magnetic colloids in the borderline between ferrofluids and magnetorheological fluids, J. Rheol. **63**, 547 (2019).
[32] J. M. Ginder, L. C. Davis, and L. D. Elie, Rheology of magnetorheological fluids: Models and measurements, Int. J. Mod. Phys. B **10**, 3293 (1996).
[33] M. R. Jolly, J. D. Carlson, and B. C. Muñoz, A model of the behaviour of magnetorheological materials, Smart Mater. Struct. **5**, 607 (1996).
[34] B. J. de Gans, H. Hoekstra, and J. Mellema, Non-linear magnetorheological behaviour of an inverse ferrofluid, Faraday Discuss. **112**, 209 (1999).
[35] Y. Shen, M. F. Golnaraghi, and G. R. Heppler, Experimental research and modeling of magnetorheological elastomers, J. Intell. Mater. Syst. Struct. **15**, 27 (2004).
[36] J. R. Morillas and J. de Vicente, Yielding behavior of model magnetorheological fluids, Soft Matter **15**, 3330 (2019).
[37] J. A. Ruiz-López, J. C. Fernández-Toledano, R. Hidalgo-Alvarez, and J. de Vicente, Testing the mean magnetization approximation, dimensionless and scaling numbers in magnetorheology, Soft Matter **12**, 1468 (2016).
[38] J. R. Morillas and J. de Vicente, Physics of magnetorheological fluids, Encycl. Smart Mater. **5**, 215 (2022).